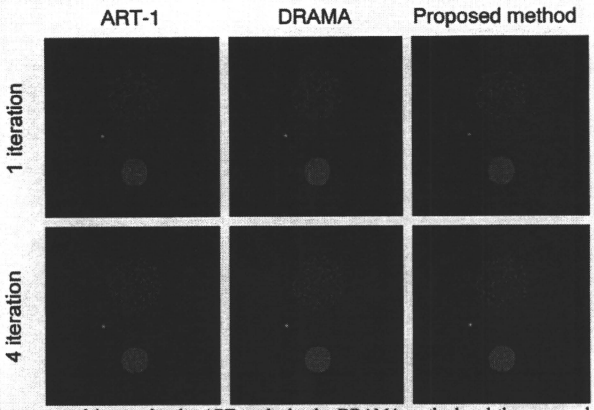

Fig.7 The reconstructed images by the ART method , the DRAMA method and the proposed method with optimal parameters.

.

Fig.6 の緩和係数の推移では, DRAMA 法と提案手法の緩和係数の値と傾向は大きく異なっているが, 反復と共に減少傾向にあり, 画像再構成の更新量を制御していることがわかる.

6. まとめ

本研究では, Row-Action 型画像再構成である ART 法に対し, 雑音伝播解析式を導出し, 画像更新により生じる雑音伝播を最小化する最適な緩和係数を提案した. 提案する緩和係数を用いる緩和法を, 固定緩和係数の ART 法, DRAMA 法の緩和係数を適用した ART 法と比較して収束性と画質の評価を行った. 評価実験の結果, DRAMA 法と提案手法は, 画像再構成の収束性と再構成画像の画質で同等な性能を示した. また, 固定緩和係数の ART 法と比較し, DRAMA 法と提案手法は収束性と画質で優れているので, リミットサイクルを防ぐ有効な緩和係数だと判断できる.

本研究では提案手法の緩和係数を画像全体で 1 つの値を用いてシミュレーション実験を行った. 今後は, 画素毎に異なる緩和係数でも性能比較実験を行い, 提案手法の改善に努めていく.

文 献

[1] Hudson HM and Larkin RS: Accelerated image reconstruction using ordered subsets of projection data. IEEE Trans Med Imag **13**: 601-609, 1994

[2] Kudo H, Nagasawa H, Saito H: Block-Gradient Method for Image Reconstruction in Emission Tomography. IEEE Trans Info Systems **J83-D-2**: 63-73, 2000

[3] Browne J and De Pierro A: A row-action alternative to the EM algorithm for maximizing likelihood in emission tomography. IEEE Trans Med Imag **15**: 687-699, 1996

[4] Tanaka E and Kudo H: Subset-dependent relaxation in block-iterative algorithms for image reconstruction in emission tomography. Phys Med Biol **48**: 1405-1422, 2003

[5] Tanaka E and Kudo H: Optimal relaxation parameters of DRAMA (dynamic RAMLA) aiming at one-pass image reconstruction for 3D-PET. Phys Med Biol **55**: 2917-2939, 2010

[6] Gordon R, Bender B, Herman GT: Algebraic reconstruction techniques(ART) for three-dimensional electron microscopy and X-ray photography. J Theor Biol **29**: 471-481, 1970

[7] Herman GT: Image reconstruction from projection. Real-Time Imaging **1**: 3-18, 1995

[8] Han G, Liang Z, You J: A fast ray-tracing technique for TCT and ECT studies. IEEE Nuclear Science Symposium 3: 1515-1518, 1999

New Method to Control the Relaxation Parameter in Row-Action Image Reconstruction Based on Analysis of Image Noise Propagation

Masakazu MATSUURA*1, Tetsuya KOBAYASHI*1, Hiroyuki KUDO*1

*1 University of Tsukuba

Image quality and convergence property of the row-action iterative reconstruction method such as algebraic reconstruction technique(ART) and dynamic RAMLA depends on the relaxation parameter that controls the amount of image update at each iteration. The relaxation parameter of DRAMA was derived from the view point of the uniform propagation of statistical noise from each subset data to the final image estimate, so that it does not depend on the amount of statistical noise in the projection data itself. In this study, we derive a noise propagation equation of the ART, and develops a new method to control the relaxation parameter which depends on the amount of statistical noise. The derivation is based on the minimization of noise propagation from the current iterate to the next iterate. In this paper, we adopt the proposed relaxation parameter to the ART due to its easiness of the noise propagation analysis, and finally compare the proposed relaxation scheme with the conventional schemes. We demonstrate that the proposed method has similar performance to that of the conventional scheme.

Key words: CT, PET, image reconstruction, ART, relaxation parameter

BRAIN RESEARCH 1369 (2011) 103–111

available at www.sciencedirect.com

ScienceDirect

www.elsevier.com/locate/brainres

BRAIN RESEARCH

Research Report

Reproducibility and variance of a stimulation-induced hemodynamic response in barrel cortex of awake behaving mice

Hiroyuki Takuwa[a,1,2,3,4], Joonas Autio[a,2,4,5], Haruka Nakayama[a,b,2,4], Tetsuya Matsuura[a,c,6], Takayuki Obata[a,6], Eiji Okada[b,1], Kazuto Masamoto[a,d,*,1,2,3,4], Iwao Kanno[a,1,3]

[a]Department of Biophysics, Molecular Imaging Center, National Institute of Radiological Sciences, 4-9-1 Anagawa, Chiba 263-8555, Japan
[b]Department of Electronics and Electrical Engineering, Keio University, 3-14-1 Hiyoshi, Kohoku-ku, Yokohama 223-8522, Japan
[c]Academic Group of Mathematical and Natural Science, Iwate University, 4-3-5 Ueda, Morioka 020-8551, Japan
[d]Center for Frontier Science and Engineering, University of Electro-Communications, 1-5-1 Chofugaoka, Chofu, Tokyo 182-8585, Japan

ARTICLE INFO

Article history:
Accepted 3 November 2010
Available online 9 November 2010

Keywords:
Cerebral blood flow
Laser-Doppler flowmetry
Neurovascular coupling
Functional plasticity
Somatosensory cortex

ABSTRACT

The present work evaluated the reproducibility and variance of the cerebral blood flow (CBF) response to natural whisker stimulation in the barrel cortex of awake behaving mice. The animal was placed on an air float ball that allowed the animal to walk, while the head of the animal was fixed in a custom-made stereotactic apparatus. Dynamic CBF changes in the barrel cortex and animal locomotion were simultaneously monitored with laser-Doppler flowmetry (LDF) and an optical motion sensor that detected the rotation distance of the ball, respectively. Whisker stimulation-induced CBF measured under daytime and nighttime conditions showed consistent responses (24% and 23% of the pre-stimulus baseline, respectively), whereas the amount of locomotion was 1.4 times higher during nighttime relative to daytime. Repeated longitudinal experiments over 7 days showed a reproducible, evoked CBF (13–26% relative to the baseline among 7 animals). The mean of the variance coefficient (i.e., standard deviation divided by mean) across multiple days was 0.11 and 0.75 for evoked CBF and locomotion, respectively. These results showed reproducible and reliable measurements of longitudinal CBF response in behaving mice regardless of day-to-day variations in locomotion. Furthermore, we confirmed that the CBF response to whisker stimulation was well localized and reproducible, measured with laser speckle imaging under awake condition. The results further show the capability of long-term hemodynamic imaging in normal and disease-

* *Corresponding author.* Center for Frontier Science and Engineering, University of Electro-Communications, 1-5-1 Chofugaoka, Chofu, Tokyo 182-8585, Japan. Fax: +81 42 443 5930.
E-mail address: masamoto@mce.uec.ac.jp (K. Masamoto).

[1] Designed research.
[2] Performed research.
[3] Wrote the paper.
[4] Analyzed data.
[5] Present address: Department of Neurobiology, A. I. Virtanen Institute, University of Kuopio, Kuopio, Finland.
[6] Helped data interpretation and discussion.

doi:10.1016/j.brainres.2010.11.007

model mice, which is of particular importance for understanding the longitudinal changes and plasticity of neurovascular coupling and behavioral performances such as during growth, development and aging.

1. Introduction

Neurovascular coupling is a fundamental process in the maintenance of normal brain function. Previous studies have attempted to understand the coupling between neural and vascular properties using *in vitro* slices and *in vivo* acute experimental models (Boorman et al., 2010; Cauli et al., 2004; Chaigneau et al., 2007; Enager et al., 2009; Lauritzen, 2001; Peppiatt et al., 2006; Shi et al., 2008; Takano et al., 2006; Zonta et al., 2003). Nevertheless, signaling pathways from neural events, such as spiking and/or synaptic activity, to vascular events, such as arterial vasodilation and/or decrease in resistance to red blood cell flow, remain incompletely understood. Additionally, the previously published studies have been conducted rather under steady state conditions, which hamper the understanding of longitudinal changes in neurovascular coupling. For example, whether dysregulation of neurovascular coupling contributes to the pathogenesis of neurodegenerative disorders remains an unanswered (Carmignoto and Gómez-Gonzalo, 2010; Lok et al., 2007; Zacchigna et al., 2008). To further understand the dynamic processing and related pathogenesis of central neurodegeneration, it is therefore important to examine the interactive evolution of neurovascular coupling from longitudinal perspectives, including such as during growth, development, and aging.

It has been shown that a development of a cerebrovascular response to neural activity lags behind an emergence of electrophysiological activity during the early postnatal period (Colonnese et al., 2008). The finding indicates a delayed formation of neurovascular coupling, which could be due to slow development of vascular reactivity and/or mediator functionality to convey neural signals to vascular reactions. On the other hand, an age-related reduction of cerebral blood flow (CBF) was known to be associated with a decline in cognitive function (Goldman et al., 1987). Later studies have suggested that the limited supply for metabolic demand is considered a key factor in the age-related decline in neural function (Riddle et al., 2003). A breakdown of microvascular networks has also been found to take place in advance of the accumulation of amyloidal plaque in a mouse model of Alzheimer's disease (Meyer et al., 2008). These studies indicate an importance for long-term investigation of the plastic changes of neurovascular coupling and associated behavioral performances with stable and reproducible animal models.

In the present study, an awake mice model was established to explore the long-term behavior of CBF and animal locomotion repeatedly while maintaining a relatively natural environment. We used laboratory mice for a series of experiments because this animal has advantages in the availability of genetically engineered disease models. The CBF response to air puff-produced whisker stimulation (10 Hz and 20 s) were examined under unanesthetized conditions because neurovascular responses are critically modulated by anesthetic agents and depths which potentially affect the reproducibility of the results (Masamoto et al., 2007; Masamoto et al., 2009). First we performed simultaneous recordings of CBF and locomotion measured with laser-Doppler flowmetry and optical motion sensor, respectively (see Fig. 1), under either daytime or nighttime conditions (*Experiment I*), to determine possible confounders arising from circadian variations in the animals (Wauschkuhn et al., 2005). We then evaluated the reproducibility and variance of the CBF response to whisker stimulation over a week, while the animals experienced a normal life between the recordings (*Experiment II*). Finally, the CBF mapping experiment was carried out with

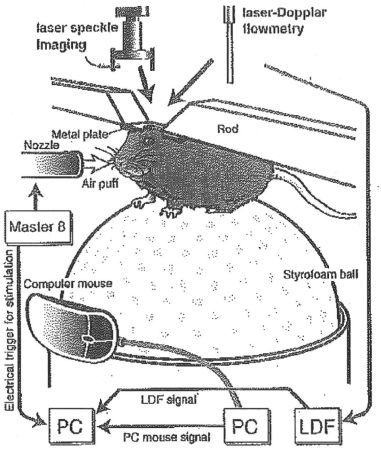

Fig. 1 – Experimental arrangement. A custom-made metal plate was attached to the animal skull and the head was fixed on a rod of a stereotactic instrument. The animal was secured on a styrofoam ball which is floated on an air jet from the bottom and the animal was allowed to walk freely on it. The rotation distance of the ball was measured with an optical computer mouse to detect animal locomotion. Either laser speckle imaging or laser-Doppler flowmetry (LDF) was performed to measure CBF in the somatosensory barrel cortex. Analog outputs converted from the computer mouse and LDF signals were recorded with a polygraph system equipped to a personal computer (PC) and synchronized with a pulse generator (Master 8) that controlled the air puff stimulation.

laser speckle imaging to validate the localization of the CBF response to whisker stimulation under awake conditions (*Experiment III*).

2. Results

2.1. *Simultaneous recordings of CBF and animal locomotion*

Fig. 2 shows the representative raw data on simultaneous recordings of CBF and locomotion obtained from single animal experiments. Upon whisker stimulation, CBF was transiently increased and had a peak of about 20% relative to baseline. The magnitude of the evoked response is distinguished relative to the baseline fluctuations (Fig. 2A). In some trials, a slight increase in baseline CBF was observed with an incidence of spontaneous grooming (i.e., self-stimulation to whiskers) (Fig. 2B). This spontaneously induced fluctuation was balanced after averaging all 8 trials and the stimulus-induced CBF change was obtained.

2.2. *Experiment I: Daytime vs. nighttime*

A comparison of the results obtained from daytime and nighttime experiments ($n=7$ animals) showed no significant differences in evoked CBF and locomotion between the two conditions (Fig. 3A and B). The mean amplitude of evoked CBF was 24±12% and 23±6% for daytime and nighttime conditions, respectively. In contrast, a slightly higher locomotion activity during pre-stimulus baseline periods was observed in nighttime relative to daytime (0.13±0.11 and 0.11±0.09, respectively), although there were no statistically significant ($P>0.05$). Population data consistently showed an equivalent response magnitude of evoked CBF (Fig. 3C) and average 1.4±0.8 times higher locomotion (Fig. 3D) during nighttime despite relatively large variations in the locomotion across seven animals.

2.3. *Experiment II: Longitudinal measurements*

A reproducible and stable response of evoked CBF was consistently observed across the 7-day experiments ($n=7$ animals). The mean amplitude of evoked CBF was 21±7%, 19±5%, 17±4% and 17±5%, on days 1, 3, 5, and 7 after operation day, respectively (Fig. 4A and 4 C). In contrast, higher variations were observed for the locomotion results. Mean of baseline locomotion was 0.09±0.09, 0.21±0.14, 0.26±0.29 and 0.11±0.11 (arbitrary unit) on days 1, 3, 5, and 7 after operation day, respectively (Fig. 4B and D). The statistically significant difference was observed for the locomotion between day 1 and day 3 (Fig. 4B and D), but not for other dates. This variation in the locomotion was mainly due to inter-subject variations across different days; 0.15±0.11, 0.23±0.17, 0.19±0.29, 0.41±0.33, 0.29±0.16, 0.20±0.20 and 0.21±0.11, averaged over 7-day experiments in individual seven subjects. Statically significant differences ($P<0.05$) were found in four of seven animals for the reproducibility of the locomotion (Fig. 4D). In contrast, the inter-subject variation in evoked CBF was considerably small; 17±2%, 16±1%, 13±1%, 14±2%, 17±1%, 26±4% and 24±3%. For the reproducibility of evoked CBF, none of the subjects showed statistical significances over 7-day experiments (Fig. 4C). Consequently, a coefficient of variance (i.e., SD / mean) for the evoked CBF measured across subjects (0.24–0.32; a median of 0.27) was two to three-times higher than that obtained for single subjects on different experiment days (0.08–0.16; a median of 0.11).

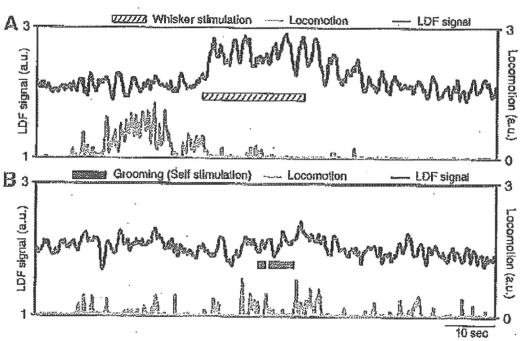

Fig. 2 – Simultaneous recordings of cerebral blood flow and locomotion. Representative raw data showed the time-course of CBF (black) and locomotion (gray) obtained from a single-trial measurement. (A) After the induction of air puff whisker stimulation (10 Hz and 20 s), a transient increase in CBF was observed. The stimulation-induced increase in CBF was readily identifiable relative to the baseline fluctuations. (B) In some trials, a slight increase in baseline CBF was observed in accordance with an incidence of spontaneous grooming, i.e., self-stimulation to whiskers (thick black bar). These random changes in baseline CBF were balanced by averaging eight stimulus trials.

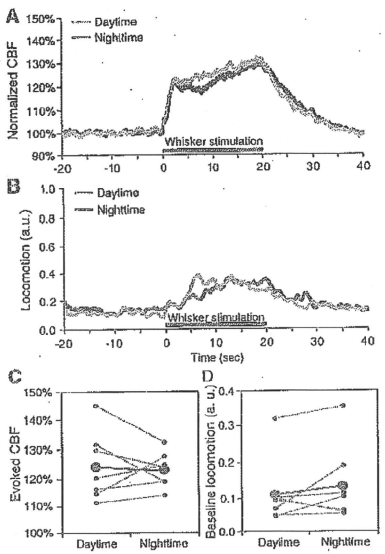

Fig. 3 – CBF and locomotion during daytime and nighttime conditions. (A) A similar time-course of CBF response to whisker stimulation (thick black bar) was observed between daytime (gray line) and nighttime (black line) conditions. CBF level was reported by normalizing the LDF signal with the pre-stimulus baseline. Each response curve represents a mean of all subject data (n=7 animals). (B) Locomotion was also similar between the two conditions but a slightly higher baseline was observed under the nighttime condition. (C) Population data showed a consistent peak amplitude of evoked CBF measured during daytime and nighttime conditions. Each dot represents data from a single animal. A bold spot and line represents the mean of all data. (D) Baseline locomotion was 1.4 times higher under the nighttime condition relative to the daytime condition, although there were no significant differences (P>0.05) between daytime and nighttime conditions.

These results consistently showed stable and reproducible measurements of evoked CBF despite the relatively large day-to-day variations in locomotion.

2.4. *Experiment III: CBF mapping*

Fig. 5A represents the intensity distribution of speckle pattern obtained during resting periods (without stimulation and no locomotion) in a representative single animal. A high intensity area in which pixel intensity represents the high mean blur rate (MBR) was observed along the cortical blood vessels visible on the surface, which is consistent with a previous report (Matsuo et al., 2008). The preserved pattern of the vascular map was reproducibly depicted after 1 week measured in the same representative animal (Fig. 5A'). Also, the well-localized CBF response to whisker stimulation was observed after dividing the frame obtained at activation peak time with pre-stimulus baseline (Fig. 5B). The activation area appeared differently from a pattern of the cortical surface

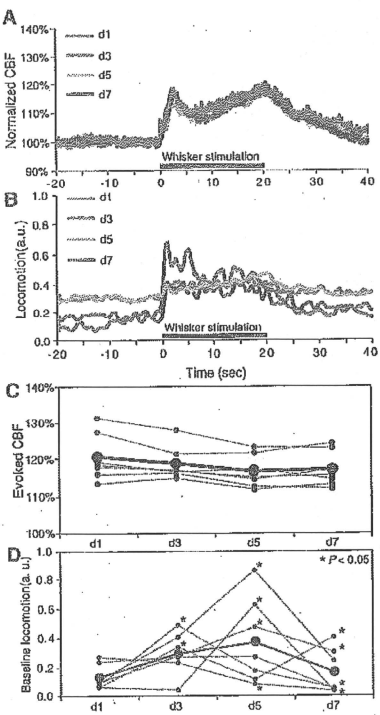

Fig. 4 – Longitudinal CBF and locomotion measurements. (A) Evoked CBF response to whisker stimulation was consistently observed from day 1 (d1) to day 7 (d7). CBF level was reported by normalizing the LDF signal with pre-stimulus baseline. Each response curve represents the mean of all data (n=7 animals). (B) In contrast, locomotion varied from day to day. (C and D) Population data consistently showed a reproducible and stable response of evoked CBF (C) despite the relatively large variations in locomotion activity (D). Each dot represents data from a single animal and a bold spot and line represents the mean of seven animal data.

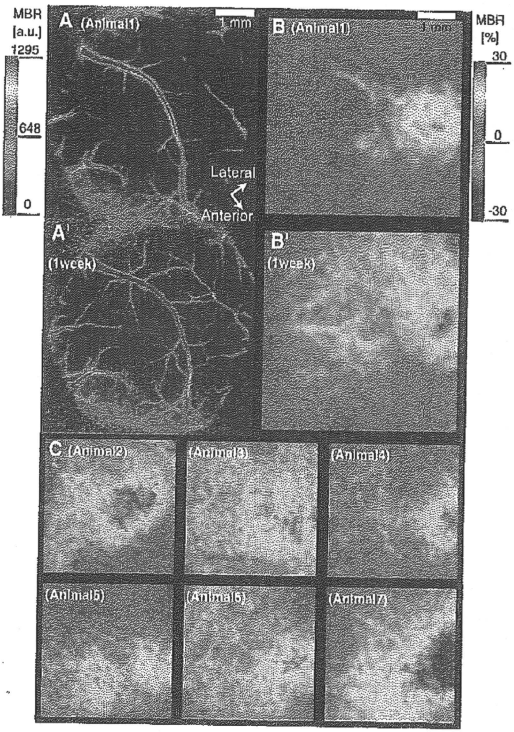

Fig. 5 – Mapping of cerebral blood flow with laser speckle imaging. (A) Representative image of speckle contrast acquired at resting condition. A vascular tree on the cortical surface appeared as high intensity pixels. Color bar indicates the mean blur rate (MBR). (B) Stimulation-induced changes in CBF obtained from the same animal shown in panel (A). Red color area indicates a large increase in CBF induced by whisker stimulation relative to pre-stimulus level. The same experiment was repeated after 1 week (A', B'). The images represent the reproducible patter of vascular tree and stimulus-induced localization of CBF response. (C) Stimulus-induced CBF map obtained from other 6 animals (animals 2–7, from left top to right down). A well-localized map of the CBF response to whisker stimulation was consistently obtained in the barrel area of the somatosensory cortex. Color bar indicates relative changes (%) in MBR from pre-stimulus baseline.

vessels (see Fig. 5A), indicating that the MBR signals arise from parenchyma microcirculation. This localized CBF response was consistently observed after 1 week (Fig. 5B'). The other 6 animals also consistently showed well-localized CBF map in the somatosensory barrel area in response to whisker stimulation (Fig. 5C). The location and sizes where the greater signal changes were observed were matched to those of the receptive field in the primary somatosensory cortex responsible to the right whiskers (Paxinos and Franklin, 2001).

3. Discussion

The present study showed a stable and reproducible response of CBF induced by whisker stimulation in awake mice in despite of variable animal locomotion between daytime and nighttime (Fig. 3) and over a week (Fig. 4). The findings indicate that the effect of locomotion on hemodynamic response in the barrel cortex is negligible. In contrast, the modulatory effect of locomotion on visually evoked cortical activity was reported in

similarly conducted awake mice experiments (Niell and Stryker, 2010). The discrepancy between that study and the present study could be due to a different cortex measured (visual vs. somatosensory cortex) and/or the differences in methodological approaches (electrophysiological recording vs. hemodynamic measurements). In rat barrel cortex, electrophysiological studies have shown a slight decrease in evoked neural response to single stimulation during voluntary motor activity relative to quiet immobility states, but highly sensitive to multiple stimuli with short intervals (i.e., high frequency) (Fanselow and Nicolelis, 1999). According to their reports, stimulation with 10 Hz, applied in the present study, induced relatively similar neural responses between with and without locomotion conditions, which is in good agreement with the present results. Another possibility is that we measured CBF as a surrogate of neural activity, whereas the previous study performed direct electrophysiological recording. The methodological differences should be considered, since it was shown that a vascular signal originates from a subset of neural population activity (Kocharyan et al., 2008). Also, nonlinear coupling between neural and vascular activity was generally known such as a threshold relationship (Nemoto et al., 2004; Nielsen and Lauritzen, 2001; Sheth et al., 2004). A correct understanding of the signal sources in hemodynamic-based neuroimaging is therefore further needed specifically for awake behaving animals.

We observed a slightly higher locomotion activity during nighttime relative to daytime (Fig. 3). This result was in good agreement with a previous report measured in Sprague–Dawley rats (Wauschkuhn et al., 2005). In our experiments, average 18% and 38% of trials detected the spontaneous locomotion (i.e., moving and/or searching) during pre-stimulus periods under daytime and nighttime conditions, respectively. This indicates that a higher locomotion observed in our results reflects a higher chance of locomotion per unit time, but less increase in walking velocity. Upon stimulation, this probability increased to 59% and 70% of trials under daytime and nighttime conditions, respectively. Although the reason why the animal starts to move associated with the stimulation onset is not clear, one may speculate that the animal felt something by the induction of stimulation and started to explore it. Although we observed higher locomotion activity under nighttime conditions, no detectable difference in CBF response was observed between both two conditions. This result further indicates that the vascular mechanism for CBF response to neural activity is locally managed, which is consistent with well-known neurovascular coupling observed in anesthetized rodents (Masamoto et al., 2007).

The pros and cons of hemodynamic neuroimaging in an awake behaving animal model should be discussed. First, awake models have advantages in the absence of possible confounding factors due to the anesthetic action on neurovascular physiology. For example, a role of nitric oxide on neurovascular coupling was reported to be different in anesthetized (α-chloralose) and unanesthetized conditions (Nakao et al., 2001). It was shown that different anesthesics and anesthesia depths produced different neurovascular coupling (Franceschini et al., 2010; Masamoto et al., 2007; Masamoto et al., 2009). Therefore, maintaining a constant level of anesthesia for a period of imaging sessions and across subjects is critically important for the reproducibility of hemodynamic imaging in anesthetized animals (Austin et al., 2005; Hyder et al., 2002). Second, awake models make it relatively easy to perform longitudinal experiments over days or weeks. Some of the anesthetic agents which are conventionally used for neurovascular coupling studies, such as α-chloralose and urethane, are not allowed for use in survival experiments. In contrast, awake models allow for repeated longitudinal measurements with a highly reproducible manner, as shown in the present results. In the present study, we found no time-dependent effects on the longitudinal CBF responses over 1-week experiments (Fig. 4), such as due to adaptation to repeated stimulation. This could be due to limited short time-window. Future studies should test the reproducibility over extended periods, i.e., several weeks and months, to probe the plastic changes in neurovascular coupling. Third, awake models have big advantages on cognitive research that are not possible under an anesthetized condition. A recent study has successfully demonstrated the motor cortex of behaving mice engaged in cognitive tasks with two-photon imaging of cellular calcium dynamics (Komiyama et al., 2010). This study shows that spatiotemporal imaging of behaving animal brain is a powerful way to understand the molecular/synaptic mechanism of cognitive functions and also the pathogenesis of neurodegenerative disorders. Finally, robust changes in hemodynamic signals induced by sensory stimuli have been consistently reported in awake condition compared to the anesthetized condition in the rodents (Berwick et al., 2002; Lahti et al., 1999; Martin et al., 2006; Peeters et al., 2001). As shown in the present study, the reproducibility and robustness of the evoked hemodynamic responses in the awake mouse barrel cortex are preferential features for longitudinal studies of neurovascular plasticity, such as during growth, development, and aging. However, behaving animal imaging has the potential drawback that i) an animal needs to be restrained which potentially stresses the animal despite adaptation to the experimental condition, ii) the image was distorted by animal motion, which becomes critical in the micro-scale of cell imaging (Dombeck et al., 2007), and iii) an imaging signal may vary depending on the active and passive sensing states (Crochet and Petersen, 2006). These drawbacks should be considered in future works with awake behaving mice.

The other advantages of using longitudinal mouse models are that mice have a short lifecycle among the species that have been used for neurovascular imaging studies. This feature enables us to track their evolution in a relatively cost-effective manner and engineer a variety of gene-manipulated animals during a comparatively short period. It should be noted that previous studies have revealed a significant contribution of specific molecules to neurovascular signal transduction using gene-knockout mouse models, such as the null mutant of nitric oxide synthase, cyclooxygenase, and tissue plasminogen activator (Kitaura et al., 2007; Ma et al., 1996; Niwa et al., 2000, 2001; Park et al., 2008; Yang et al., 2003). Further studies of longitudinal neurovascular and related behavioral measurements with gene-manipulated mouse models would provide

valuable information on the pathogenesis and therapeutic approaches in a variety of neural disorders (Mayanagi et al., 2008; Takeda et al., 2009).

4. Experimental procedures

4.1. Animal preparation

A total of 21 male C57BL/6 J mice (20–30 g, 7–11 weeks; Japan SLC, Inc, Hamamatsu) were used in three separate experiments: daytime-nighttime experiments (*Experiment I*, n=7), longitudinal experiments (*Experiment II*, n=7), and CBF mapping experiments (*Experiment III*, n=7). The animals were housed in a 12-hour dark and 12-hour light cycle room at a temperature of 25 °C with ad libitum water and feed. All experimental protocols followed the institutional guideline on humane care and use of laboratory animals and were approved by the Institutional Committee for Animal Experimentation.

For the surgical procedure, animals were anesthetized with a mixture of air, oxygen, and isoflurane (3–5% for induction, and 2% for surgery) through a facemask. The animals were fixed in a stereotactic frame and the rectal temperature was maintained at 38 °C using a heating pad (ATC-210, Unique Medical Co. Ltd., Japan). A midline incision (10 mm) was made to expose the skull over the left somatosensory cortex. The skull (3 mm by 3 mm centered at 1.8 mm caudal and 2.5 mm lateral from the bregma) was thinned to translucency using a dental drill. A custom-made metal plate with a 7-mm diameter hole in the center was attached to the skull with dental resin. After completion of the surgery, the animals were allowed to recover from anesthesia and housed for at least 1 day before initiation of the experiments.

4.2. Experimental protocols

Animals were initially anesthetized with 1–2% isoflurane to fix the animals in the experiment apparatus. A head plate mounted on the animal's skull was attached to a custom-made stereotactic apparatus (Fig. 1) in reference to the method of Dombeck et al. (2007). Animals were secured on a ball (98 mm in outer diameter) made of styrofoam (9 g) and then the isoflurane anesthesia was discontinued. The ball was floated in inside perforated cup (100 mm in inner diameter) by a jet of air produced with a motor-powered propeller from beneath the cup. This allowed for the animals to exercise freely on the ball while the animal's head was fixed in an apparatus. An air outlet (4 mm in inner diameter) was placed in front of the tip of the nose at a distance of 10–20 mm. An air puff was delivered to the entire right whiskers at a pressure of ~15 psi via a compressed air bottle. A rectangular pulse stimulation (50-ms pulse width and 100-ms onset-to-onset interval, i.e., 10-Hz frequency) generated with a Master-8 (A.M.P.I) was induced for a 20-s duration. In each experiment, eight consecutive trials were repeated with an onset-to-onset interval of 120 s. The recording was started after approximately 30 min from the cessation of anesthesia to stabilize the experimental conditions. The recording took 30 min including 10 min for resting baseline measurements (without whisker stimulation).

Three experiments were conducted in three separate groups of awake animals. In *Experiment I*, CBF and animal locomotion were compared between daytime (12 pm to 2 pm) and nighttime (12 am to 2 am) conditions. In *Experiment II*, CBF and locomotion were measured every other day for 7 days. In *Experiment III*, CBF mapping in response to whisker stimulation was performed. In some experiments, animal behavior (e.g., grooming, self-motion of whiskers, and rest) during recording was also videotaped with a digital camera for later reference.

4.3. Locomotion detection

Animal locomotion was measured by monitoring rotation of the ball on which the animal was placed (Fig. 1). Rotational position was detected using an optical computer mouse with a spatial resolution of 0.3 mm in the X–Y axis every 0.1 s. Walking distance of the animal was then calculated with custom-built software and the digitalized information was sent to a polygraph data acquisition system (MP150, BIOPAC Systems, Inc., Goleta, CA) via digital-analog converter. The data on walking distance were recorded at a rate of 100 Hz with data acquisition software (AcqKnowledge, Biopac Systems, Inc., Goleta, CA).

4.4. Laser–Doppler flowmetry

Dynamic changes in CBF were monitored with laser-Doppler flowmetry (FLO-C1, OMEGAWAVE, Inc., Tokyo, Japan). The tip of the LDF probe (Type NS, OMEGAWAVE, Inc., Tokyo, Japan) was positioned on the thinned skull perpendicular to the surface of the brain while avoiding large blood vessel areas. The activated hot spot was preliminarily determined by screening the response to whisker stimulation at several points in the somatosensory area. Then, the X–Y position of the LDF tip was marked on the edge of the cranial window for reproducible placement of the LDF tip. The angle of the LDF probe to the cortex was fixed with the manipulator, perpendicular to the thinned skull surface. Also, the distance between LDF tip and surface of the cranial window was maintained among the different experiments. In each experiment, the consistent level of the reflected light signal for the LDF measurements was confirmed before initiation of the recording. A time constant of the LDF instrument was 0.1 s, and the LDF value (i.e., a representation of CBF) was recorded with analog data recorder (AcqKnowledge, Biopac Systems, Inc., Goleta, CA) at a rate of 200 Hz.

4.5. Laser speckle imaging

CBF mapping was performed using a laser speckle imaging technique as previously described (Matsuo et al., 2008). The thinned skull area was illuminated with a laser diode at 780-nm wavelength, and reflected light was measured with a CCD camera (400 by 400 pixels) from the top of the cortex (dorsal view) through a microscope. Because a speckle pattern gets blurred with an increase in motion (i.e., red blood cell speed), the mean blur rate (MBR) was measured to map CBF level (Konisi et al., 2002). Four by four adjacent pixels with six consecutive frames were used to calculate MBR (Matsuo et al., 2008), resulting in an image resolution of 100 by 100 pixels and

a frame rate of five frames per second. Stimulation-induced CBF responses were represented by dividing the MBR in each frame with that of the frame just before the onset of stimulation on a pixel by pixel basis. Since laser speckle technique is sensitive to movement of the illuminated cortex (i.e., motion artifacts), this technique is suited to validate the localization and quality of hemodynamic imaging in awake behaving animals.

4.6. *Data analysis*

CBF and locomotion signals were simultaneously recorded using a biopac system that was synchronized with Master 8 at the onset of whisker stimulation (Fig. 1). CBF and locomotion data were analyzed offline. For the CBF time-course data, the LDF signal was first down-sampled to 40 Hz to reduce data size and random noise, and normalized toward a baseline level (20-s pre-stimulus data) in each trial. The time-course data in each trial was then averaged across all trials in each animal. Evoked CBF amplitude was reported by measuring the peak value within 5 s after the onset of stimulation and was represented as a % change relative to the pre-stimulus baseline. Locomotion was measured by calculating the mean walking distance (per 0.1 s) during pre-stimulus baseline periods (20 s) in each trial and averaged for all trials in each animal. For the statistical analysis, student's t-tests were performed for data of subject to subject variations between daytime and nighttime in *Experiment I*, across different days (vs. day 1) in *Experiment II*, and also data of inter-subject variations across different days (vs. day 1) for the reproducibility experiments in *Experiment II*. The obtained values are reported as the mean±standard deviation if not otherwise specified.

Role of the funding source

The study was supported by Special Coordination Funds for Promoting Science and Technology (K.M.), and KAKENHI from Japan Society for the Promotion of Science in Japan (T.O.). There are no roles of the sponsors on the conduct of the research or preparation of the article.

Conflict of interest

The authors declare no conflict of interest.

Acknowledgments

The authors thank Dr. Hiroshi Kawaguchi, Ms. Kyoko Yamazaki, Mr. Naotaka Sakashita, and Mr. Kosaku Tsujii for discussion and assistance with the experiments.

REFERENCES

Austin, V.C., Blamire, A.M., Allers, K.A., Sharp, T., Styles, P., Matthews, P.M., Sibson, N.R., 2005. Confounding effects of anesthesia on functional activation in rodent brain: a study of halothane and alpha-chloralose anesthesia. NeuroImage 24, 92–100.

Berwick, J., Martin, C., Martindale, J., Jones, M., Johnston, D., Zheng, Y., Redgrave, P., Mayhew, J., 2002. Hemodynamic response in the unanesthetized rat: intrinsic optical imaging and spectroscopy of the barrel cortex. J. Cereb. Blood Flow Metab. 22, 670–679.

Boorman, L., Kennerley, A.J., Johnston, D., Jones, M., Zheng, Y., Redgrave, P., Berwick, J., 2010. Negative blood oxygen level dependence in the rat: a model for investigating the role of suppression in neurovascular coupling. J. Neurosci. 30, 4285–4294.

Carmignoto, G., Gómez-Gonzalo, M., 2010. The contribution of astrocyte signalling to neurovascular coupling. Brain Res. Rev. 63, 138–148.

Cauli, B., Tong, X.K., Rancillac, A., Serluca, N., Lambolez, B., Rossier, J., Hamel, E., 2004. Cortical GABA interneurons in neurovascular coupling: relays for subcortical vasoactive pathways. J. Neurosci. 24, 8940–8949.

Chaigneau, E., Tiret, P., Lecoq, J., Ducros, M., Knöpfel, T., Charpak, S., 2007. The relationship between blood flow and neuronal activity in the rodent olfactory bulb. J. Neurosci. 27, 6452–6460.

Colonnese, M.T., Phillips, M.A., Constantine-Paton, M., Kaila, K., Jasanoff, A., 2008. Development of hemodynamic responses and functional connectivity in rat somatosensory cortex. Nat. Neurosci. 11, 72–79.

Crochet, S., Petersen, C.C., 2006. Correlating whisker behavior with membrane potential in barrel cortex of awake mice. Nat. Neurosci. 9, 608–610.

Dombeck, D.A., Khabbaz, A.N., Collman, F., Adelman, T.L., Tank, D.W., 2007. Imaging large-scale neural activity with cellular resolution in awake, mobile mice. Neuron 56, 43–57.

Enager, P., Piilgaard, H., Offenhauser, N., Kocharyan, A., Fernandes, P., Hamel, E., Lauritzen, M., 2009. Pathway-specific variations in neurovascular and neurometabolic coupling in rat primary somatosensory cortex. J. Cereb. Blood Flow Metab. 29, 976–986.

Fanselow, E.E., Nicolelis, M.A., 1999. Behavioral modulation of tactile responses in the rat somatosensory system. J. Neurosci. 19, 7603–7616.

Franceschini, M.A., Radhakrishnan, H., Thakur, K., Wu, W., Ruvinskaya, S., Carp, S., Boas, D.A., 2010. The effect of different anesthetics on neurovascular coupling. NeuroImage 51, 1367–1377.

Goldman, H., Berman, R.F., Gershon, S., Murphy, S.L., Altman, H.J., 1987. Correlation of behavioral and cerebrovascular functions in the aging rat. Neurobiol. Aging 8, 409–416.

Hyder, F., Rothman, D.L., Shulman, R.G., 2002. Total neuroenergetics support localized brain activity: implications for the interpretation of fMRI. Proc. Natl Acad. Sci. USA 99, 10771–10776.

Kitaura, H., Uozumi, N., Tohmi, M., Yamazaki, M., Sakimura, K., Kudoh, M., Shimizu, T., Shibuki, K., 2007. Roles of nitric oxide as a vasodilator in neurovascular coupling of mouse somatosensory cortex. Neurosci. Res. 59, 160–171.

Kocharyan, A., Fernandes, P., Tong, X.K., Vaucher, E., Hamel, E., 2008. Specific subtypes of cortical GABA interneurons contribute to the neurovascular coupling response to basal forebrain stimulation. J. Cereb. Blood Flow Metab. 28, 221–231.

Komiyama, T., Sato, T.R., O'Connor, D.H., Zhang, Y.X., Huber, D., Hooks, B.M., Gabitto, M., Svoboda, K., 2010. Learning-related fine-scale specificity imaged in motor cortex circuits of behaving mice. Nature 464, 1182–1186.

Konisi, N., Tokimoto, Y., Kohra, K., Fuji, H., 2002. New laser speckle flowgraphy system using CCD camera. Opt. Rev. 9, 163–169.

Lahti, K.M., Ferris, C.F., Li, F., Sotak, C.H., King, J.A., 1999. Comparison of evoked cortical activity in conscious and

propofol-anesthetized rats using functional MRI. Magn. Reson. Med. 41, 412–416.
Lauritzen, M., 2001. Relationship of spikes, synaptic activity, and local changes of cerebral blood flow. J. Cereb. Blood Flow Metab. 21, 1367–1383.
Lok, J., Gupta, P., Guo, S., Kim, W.J., Whalen, M.J., van, Leyen, K., Lo, E.H., 2007. Cell-cell signaling in the neurovascular unit. Neurochem. Res. 32, 2032–2045.
Ma, J., Ayata, C., Huang, P.L., Fishman, M.C., Moskowitz, M.A., 1996. Regional cerebral blood flow response to vibrissal stimulation in mice lacking type I NOS gene expression. Am. J. Physiol. 270, 1085–1090.
Martin, C., Martindale, J., Berwick, J., Mayhew, J., 2006. Investigating neural-hemodynamic coupling and the hemodynamic response function in the awake rat. Neuroimage 32, 33–48.
Masamoto, K., Kim, T., Fukuda, M., Wang, P., Kim, S.G., 2007. Relationship between neural, vascular, and BOLD signals in isoflurane-anesthetized rat somatosensory cortex. Cereb. Cortex 17, 942–950.
Masamoto, K., Fukuda, M., Vazquez, A., Kim, S.G., 2009. Dose-dependent effect of isoflurane on neurovascular coupling in rat cerebral cortex. Eur. J. Neurosci. 30, 242–250.
Matsuo, S., Sakaguchi, K., Katsura, T., Yamazaki, K., Kawaguchi, H., Maki, A., Fujii, H., Okada, E., 2008. Measurement of distribution of blood-flow change in exposed cortex by laser speckle flowgraphy. The Review of Laser Engineering Supplemental Volume 2008. 36, 1339–1342.
Mayanagi, K., Katakam, P.V., Gáspár, T., Domoki, F., Busija, D.W., 2008. Acute treatment with rosuvastatin protects insulin resistant (C57BL/6 J ob/ob) mice against transient cerebral ischemia. J. Cereb. Blood Flow Metab. 28, 1927–1935.
Meyer, E.P., Ulmann-Schuler, A., Staufenbiel, M., Krucker, T., 2008. Altered morphology and 3D architecture of brain vasculature in a mouse model for Alzheimer's disease. Proc. Natl Acad. Sci. USA 105, 3587–3592.
Nakao, Y., Itoh, Y., Kuang, T.Y., Cook, M., Jehle, J., Sokoloff, L., 2001. Effects of anesthesia on functional activation of cerebral blood flow and metabolism. Proc. Natl Acad. Sci. USA 98, 7593–7598.
Nemoto, M., Sheth, S., Guiou, M., Pouratian, N., Chen, J.W., Toga, A. W., 2004. Functional signal- and paradigm-dependent linear relationships between synaptic activity and hemodynamic responses in rat somatosensory cortex. J. Neurosci. 24, 3850–3861.
Niell, C.M., Stryker, M.P., 2010. Modulation of visual responses by behavioral state in mouse visual cortex. Neuron 65, 472–479.
Nielsen, A.N., Lauritzen, M., 2001. Coupling and uncoupling of activity-dependent increases of neuronal activity and blood flow in rat somatosensory cortex. J. Physiol. 533, 773–785.
Niwa, K., Araki, E., Morham, S.G., Ross, M.E., Iadecola, C., 2000. Cyclooxygenase-2 contributes to functional hyperemia in whisker-barrel cortex. J. Neurosci. 20, 763–770.
Niwa, K., Haensel, C., Ross, M.E., Iadecola, C., 2001. Cyclooxygenase-1 participates in selected vasodilator responses of the cerebral circulation. Circ. Res. 88, 600–608.
Park, L., Gallo, E.F., Anrather, J., Wang, G., Norris, E.H., Paul, J., Strickland, S., Iadecola, C., 2008. Key role of tissue plasminogen activator in neurovascular coupling. Proc. Natl Acad. Sci. USA 105, 1073–1078.
Paxinos, G., Franklin, K.B.J., 2001. The mouse brain in stereotaxic coordinates. Academic Press.
Peeters, R.R., Tindemans, I., De Schutter, E., Van der Linden, A., 2001. Comparing BOLD fMRI signal changes in the awake and anesthetized rat during electrical forepaw stimulation. Magn. Reson. Imaging 19, 821–826.
Peppiatt, C.M., Howarth, C., Mobbs, P., Attwell, D., 2006. Bidirectional control of CNS capillary diameter by pericytes. Nature 443, 700–704.
Riddle, D.R., Sonntag, W.E., Lichtenwalner, R.J., 2003. Microvascular plasticity in aging. Ageing Res. Rev. 2, 149–168.
Sheth, S.A., Nemoto, M., Guiou, M., Walker, M., Pouratian, N., Toga, A.W., 2004. Linear and nonlinear relationships between neuronal activity, oxygen metabolism, and hemodynamic responses. Neuron 42, 347–355.
Shi, Y., Liu, X., Gebremedhin, D., Falck, J.R., Harder, D.R., Koehler, R.C., 2008. Interaction of mechanisms involving epoxyeicosatrienoic acids, adenosine receptors, and metabotropic glutamate receptors in neurovascular coupling in rat whisker barrel cortex. J. Cereb. Blood Flow Metab. 28, 111–125.
Takano, T., Tian, G.F., Peng, W., Lou, N., Libionka, W., Han, X., Nedergaard, M., 2006. Astrocyte-mediated control of cerebral blood flow. Nat. Neurosci. 9, 260–267.
Takeda, S., Sato, N., Takeuchi, D., Kurinami, H., Shinohara, M., Niisato, K., Kano, M., Ogihara, T., Rakugi, H., Morishita, R., 2009. Angiotensin receptor blocker prevented beta-amyloid- induced cognitive impairment associated with recovery of neurovascular coupling. Hypertension 54, 1345–1352.
Wauschkuhn, C.A., Witte, K., Gorbey, S., Lemmer, B., Schilling, L., 2005. Circadian periodicity of cerebral blood flow revealed by laser-Doppler flowmetry in awake rats: relation to blood pressure and activity. Am. J. Physiol. Heart Circ. Physiol. 289, 1662–1668.
Yang, G., Zhang, Y., Ross, M.E., Iadecola, C., 2003. Attenuation of activity-induced increases in cerebellar blood flow in mice lacking neuronal nitric oxide synthase. Am. J. Physiol. Heart Circ. Physiol. 285, 298–304.
Zacchigna, S., Lambrechts, D., Carmeliet, P., 2008. Neurovascular signalling defects in neurodegeneration. Nat. Rev. Neurosci. 9, 169–181.
Zonta, M., Angulo, M.C., Gobbo, S., Rosengarten, B., Hossmann, K.A., Pozzan, T., Carmignoto, G., 2003. Neuron-to-astrocyte signaling is central to the dynamic control of brain microcirculation. Nat. Neurosci. 6, 43–50.

RADIATION RESEARCH 175, 1–9 (2011)
0033-7587/11 $15.00

DOI: 10.1667/RR2134.1

Quantitative and Noninvasive Assessment of Prenatal X-Ray-Induced CNS Abnormalities Using Magnetic Resonance Imaging

Shigeyoshi Saito,[a,b] Ichio Aoki,[b,1] Kazuhiko Sawada,[c] Xue-Zhi Sun,[d] Kai-Hsiang Chuang,[e] Jeff Kershaw,[b] Iwao Kanno[b] and Tetsuya Suhara[a,b]

[a] *Department of Molecular and Neuroimaging, Graduate School of Medicine, Tohoku University, Sendai, Japan;* [b] *Molecular Imaging Center, National Institute of Radiological Sciences, Chiba, Japan;* [c] *Laboratory of Anatomy, Department of Physical Therapy, Faculty of Medical and Health Sciences, Tsukuba International University, Tsuchiura, Japan;* [d] *Regulation Science Research Group, National Institute of Radiological Sciences, Chiba, Japan; and* [e] *Singapore Bioimaging Consortium, Singapore*

Saito, S., Aoki, I., Sawada, K., Sun, X-Z., Chuang, K-H., Kershaw, J., Kanno, I. and Suhara, T. Quantitative and Noninvasive Assessment of Prenatal X-Ray-Induced CNS Abnormalities Using Magnetic Resonance Imaging. *Radiat. Res.* 175, 1–9 (2011).

Our purpose was to noninvasively assess formation of the microvasculature, blood-brain barrier (BBB) and blood-CSF barrier formation of prenatal X-ray-induced CNS abnormalities using quantitative MRI. Eight pregnant female Sprague-Dawley rats were divided into two groups consisting of control and X-irradiated animals. After birth, 20 neonatal male rats were divided into four groups of five rats. To evaluate the development of the BBB, changes in T_1 induced by Gd-DTPA were compared quantitatively in normal and prenatally irradiated animals in the formative period 1 to 2 weeks after birth. To assess the abnormalities of the microvasculature, quantitative perfusion MRI and MR angiography were also used. Histology was also performed to evaluate the BBB (albumin) and vascular endothelial cells (laminin). Decreased cerebral blood flow (CBF) and angioarchitectonic abnormalities were observed in the prenatally irradiated rats. However, abnormalities of the BBB and blood-CSF barrier were not observed using Gd-enhanced MRI and albumin staining. Quantitative perfusion MRI, MR angiography and Gd-enhanced T_1 mapping are useful for assessing CNS disturbance after prenatal exposure to radiation. These techniques provide important diagnostic information for assessing the condition of patients during the early stages of life after accidental or unavoidable prenatal exposure to radiation. © 2011 by Radiation Research Society

INTRODUCTION

Many studies of the prenatally radiation-exposed survivors of the atomic bombings of Hiroshima and Nagasaki show that exposure to ionizing radiation during pregnancy has harmful effects on the development of the human central nervous system (CNS) (*1–3*). It is also known that the animal embryo is sensitive to radiation. For example, irradiation of a fertilized egg with as little as 0.1 Gy is lethal, while exposure of an embryo to radiation can cause various diseases such as hydrocephalus and microcephaly (*3*), both of which have been observed in animal models after prenatal X irradiation at day 15 of pregnancy in rats and day 13 in mice (*4*). Developmental disorders such as hippocampus atrophy and ventricle dilatation have been found in rats after prenatal radiation exposure (*5, 6*). Those studies focused on observing morphological alterations in injury model rats using immunohistochemical staining and behavior analysis (*5, 6*). Further investigation and noninvasive assessment of CNS damage after irradiation during the prenatal stage is important not only for understanding the biological effects of X radiation but also for emergency treatment and diagnosis after accidental irradiation.

The CNS of the fetus is sensitive to radiation (*13*), but the CNS of adult animals is more resistant. Nevertheless, a high dose of ionizing radiation (15–20 Gy) can cause cellular heterogeneity, spinal cord myelopathy, white matter necrosis (leukoencephalopathy), and microvascular damage (*7, 8*) in the CNS of adult mice. Microvascular damage causes increased endothelial cell swelling, vascular permeability and edema, lymphocyte adhesion and infiltration, and apoptosis (*9*) in the acute phase. In one study, 20% of the apoptotic cells observed after a dose of radiation over 50 Gy were endothelial cells in the CNS of 16-week-old mice (*8*). Disruption of the blood-brain barrier (BBB) and blood-cerebral spinal fluid (CSF) barrier were found to be the primary early effects after X-ray exposure of the adult rat spinal cord (15 Gy) and rat brain (60 Gy) (*10, 11*). Yuan *et al.* characterized the short- and long-term effects of fractionated radiotherapy (total dose 40 Gy) on the cerebral microvasculature and also investigated the mechanisms altering BBB permeability in 6–7-week-old

[1] Address for correspondence: Molecular Imaging Center, National Institute of Radiological Sciences, Anagawa 4-9-1, Inage, Chiba, Chiba 263-8555 Japan; e-mail: aoki@nirs.go.jp.

mice (*12*). They found that changes in BBB permeability increased with radiation exposure in the adult rodent. In the chronic stage, microvascular disorders such as capillary collapse, teleangiectasias and fibrous scarring have been observed (*7*). Therefore, recovery of brain perfusion should be a primary target in the treatment of radiation injury and radiotherapy in the adult. On the other hand, the BBB is immature during the early stages after birth (*14*). Although many studies have investigated CNS damage after irradiation in adult animals, no study has examined damage to the BBB, blood-CSF barrier and microvasculature of the CNS in a rodent model of prenatal radiation exposure.

MRI is useful for detecting physiological changes after radiation exposure (*15–17*). For example, diffusion-weighted MRI and the apparent diffusion coefficient (ADC) are useful tools for detecting radiation-induced spinal cord degeneration (*15*) and tissue necrosis (*16*) without an exogenous contrast agent. MR angiography can detect delayed vascular injury induced by a single high dose of X rays applied to the rat brain (*17*), and dynamic susceptibility contrast-enhanced perfusion MRI showed the dose-dependent derangement in the chronic phase of radiation-induced injury (*18*). To assess the BBB alterations in an ischemia model, a rapid quantitative T_1-mapping method using Look-Locker acquisition was recently established to allow quantitative evaluation and intersubject comparison of the dynamics of T_1 contrast agents (*19*). Gd-chelates such as Gd-DTPA act as intravascular and extracellular T_1 agents when introduced to the CNS. In neonatal rats, the BBB matures at 2 weeks after birth (*20*). If the BBB is immature, Gd-DTPA can leak from the capillaries but is unable to enter cells. We expect that quantitative T_1 measurements after Gd-DTPA administration and assessment of cerebral microvasculature perfusion with MRI will provide important information for research into CNS development after radiation exposure.

Our goal in this study was to noninvasively assess morphological alterations, BBB and blood-CSF barrier integrity, and microvasculature of X-ray-induced CNS abnormalities in prenatally irradiated rats using quantitative MRI. To evaluate the development of the BBB, the distribution of Gd-DTPA in the CNS was compared quantitatively in normal and prenatally irradiated rats in the formative period 1 to 2 weeks after birth. To assess the microvasculature and angioarchitecture in the CNS, quantitative perfusion MRI and MR angiographs were also acquired. Histological analysis was also performed to evaluate the BBB (albumin staining) and vascular endothelial cells (laminin). We found that decreased cerebral blood flow (CBF) induced by abnormal capillaries and arteries in the irradiated neonatal rats can be assessed *in vivo* using perfusion MRI. Such angioarchitectonic abnormalities revealed by noninvasive and quantitative imaging technology can provide diagnostic information about patients, in particular children and fetuses, who have been exposed to radiation through misalignment of X-ray equipment, the side effects of radiation therapy (e.g. telangiectasia, cavernous angioma, radiation-induced cryptic vascular malformation), an accident at a nuclear plant, or nuclear terrorism/explosion.

MATERIALS AND METHODS

Animal Procedures

The Animal Welfare Committee of the National Institute of Radiological Sciences (NIRS) approved this study. Pregnant female Sprague-Dawley rats (n = 8, 250–280 g, Japan SLC, Hamamatsu, Japan) were allowed to rest for 1 week before the experiment. The animals had free access to food and water and were kept under standard laboratory conditions of 22–23°C room temperature, around 50% humidity, and a 12/12-h light/dark cycle. The eight pregnant female rats were divided into two groups consisting of four control and four radiation-exposed animals. The irradiated group received a single exposure to whole-body X radiation at a dose of 1.5 Gy on day 15 of pregnancy (*5, 21*). X-irradiation conditions were 200 kVp, 20 mA, 0.5-mm copper + 0.5-mm aluminum filter, 110-cm distance from focus to object, and 0.27–0.28 Gy/min dose rate (*5*). After birth, 20 neonatal male rats were selected at random from both the normal and radiation-exposed animals. The male rats were arranged into four groups of five rats for MRI experiments: (1) 1-week-old normal rats (12.6 ± 0.7 g), (2) 2-week-old normal rats (25.1 ± 0.8 g), (3) 1-week-old radiation-exposed rats (11.0 ± 0.7 g), and (4) 2-week-old radiation-exposed rats (22.9 ± 0.9 g). For all groups, the angioarchitecture and CBF were evaluated using MR angiography and perfusion imaging, respectively. Both control and radiation-exposed neonatal rats were kept with the mother rats in regular light/dark cycles until the MRI experiments were performed either 1 or 2 weeks after birth. The body weights of the radiation-exposed rats were significantly lower than those of the normal rats for both the 1- and 2-week old animals ($P < 0.001$).

MRI Measurements

All MRI experiments were performed on a 7.0 T MRI scanner (Magnet: Kobelco and JASTEC Japan; Console: Bruker Biospin, Germany) with a volume coil for transmission (Bruker) and 2-channel phased array coil for reception (Rapid Biomedical, Germany). Immediately prior to and during the MRI scan, all rats were anesthetized with 2.0% isoflurane (Abbott Japan). Rectal temperature was monitored continuously and was maintained at 36.5 ± 0.5°C using a heating pad. During MRI scanning, the rats lay in a prone position on an MRI-compatible cradle and were held in place with handmade ear bars. Anesthesia was given to the animal through a face mask. The center of the imaging slices was carefully set at bregma −0.36 mm with reference to the Paxinos rat brain atlas (*22*).

MRI Experiment

MR angiography. MR angiography was performed using a 3D-FLASH sequence to compare the condition of the vascular system only for the normal and 2-week-old radiation-exposed rats. [TR = 15 ms, TE = 2.4 ms, flip angle = 20°, field-of-view (FOV) = 25.6 × 19.2 × 19.2 mm^2, matrix = 256 × 192 × 192, scan time = 27 min 38 s).

Perfusion MRI. Quantitative perfusion imaging was performed using the FAIR (flow-sensitive alternating inversion-recovery) arterial spin-labeling method (*23*) with echo-planar imaging (EPI) readout (3 slices, slice thickness = 2 mm, FOV = 22.4 × 22.4 mm, matrix = 128 × 64, number of repetitions = 2, TR = 18,000 ms, TE = 26 ms, scan

time = 4 min 12 s). Two quantitative T_1 data sets were acquired. The first T_1 series used selective inversion and the second T_1 series used nonselective inversion. The apparent T_1 was calculated for each image series, and then the CBF was estimated using the equation $CBF = \lambda (1/T_{1\text{selective}} - 1/T_{1\text{nonselective}})$, where the blood-brain partition coefficient λ was set to 90 ml/100 g (*23*). To minimize anesthetic loading and maintain the health of the 1-week-old animals during the experiment, the MR angiography and perfusion MRI were acquired only for the 2-week-old group.

Gd-enhanced T_1-weighted MRI and quantitative T_1 mapping. Gd-DTPA (Magnevist, 0.004 ml/g, 50 m*M*, Bayer) was used to assess BBB integrity by injecting it into a tail vein during continuous and repeated T_1-weighted MRI and T_1-mapping acquisitions. Coronal multi-slice T_1-weighted MR images (T_1WI) were acquired with a spin-echo (SE) sequence (TR/TE = 400/9.57 ms, 5 slices, slice thickness = 1.0 mm, matrix = 256 × 256, FOV = 25.6 × 25.6 mm², average = 4), and T_1 mapping was performed with a 2D Look-Locker sequence (TR/TE = 10000/10 ms, 5 slices, slice thickness = 1.0 mm, matrix = 64 × 32, FOV = 25.6 × 12.8 mm², average = 1). For the T_1 mapping, eight scans with the same parameters were acquired repeatedly over a period of 42 min 50 s.

Histology

Immediately after MRI scanning, all rats were killed humanely with an overdose of pentobarbital (Dainippon Sumitomo Pharma Co., Ltd, Japan) and prepared for histology by perfusion-fixation with saline containing heparin followed by 4% paraformaldehyde. The extracted brains were embedded in paraffin and, with reference to the Paxinos rat brain atlas (*22*), coronal slices (40 μm thick) were cut corresponding to bregma −0.36 mm. Slices were stained with albumin (*24*) and laminin (*25*) and then examined using light microscopy. Albumin staining is used as a marker of BBB leakage (*24*). To assess BBB integrity, we analyzed a randomly selected 0.04-mm² area in the dorsal cortex and calculated the ratio of albumin-stained area to nonstained area. The area containing albumin-positive cells was identified in the cortex area of the immunohistochemical images as follows: (*1*) the brightness and contrast were optimized automatically using Adobe Photoshop (Ver. 8.0.1), (*2*) the brown-stained positive cells were enhanced and converted to a black-and-white binary map using a 50% intensity threshold, (*3*) the total area of the black regions of the binary map was measured using NIH ImageJ (Ver.1.40g), and (*4*) the ratio of positive cell area to total area was calculated. The number of positive cells per mm² of cortex was calculated from the laminin-stained slices. The immunohistochemical staining results were compared between groups using one-way ANOVA with Tukey's correction. The statistical significance was set to $P < 0.05$.

MRI Data Analysis and Statistics

Figure 1-A1 shows the ROIs defined in the dorsal cortex (from the primary motor cortex to secondary somatosensory) with reference to the Paxinos rat brain atlas (*22*). The diameter of the middle cerebral artery (MCA) was estimated from the full-width half-maximum of the vessel profile at its origin (ParaVision 4.0, Bruker Biospin and Image J). All statistical analysis was performed using Prism 5 (Version 5, GraphPad Software). Two-way ANOVA with the Bonferroni correction was applied to compare changes in the normalized T_1 values across groups of animals. $P < 0.05$ was considered significant. Similarly, an unpaired *t* test was applied to compare body weight, CBF, blood-CSF barrier and blood vessel diameter between the normal and radiation-exposed groups. The brain size was evaluated manually in a slice approximately −0.36 mm posterior to the bregma and in the same orientation as the MR images based on Paxinos's mouse brain atlas (*22*). To evaluate changes in T_1 and CBF, the ROI was defined as the dorsal cortex (from the primary motor cortex to secondary somatosensory cortex) to minimize signal inhomogeneity. T_1 values were normalized using the T_1 map acquired immediately before injection of the contrast agent. The T_1 ratio was calculated as the ratio of [cortical T_1 values after Gd-DTPA injection]/[cortical T_1 values before Gd-DTPA injection]. The T_1 ratio in the CNS reflects the permeability of the BBB to Gd-DTPA. A low T_1 ratio suggests a higher local Gd-DTPA concentration and greater BBB permeability (disruption or immaturity). To assess the permeability of the blood-CSF barrier, the Gd-DTPA enhancement ratio in the ventricles was calculated as the ratio of the [Signal intensity of T_1-weighted images in the ventricles after Gd-DTPA injection]/[Signal intensity of T_1-weighted images in the ventricles before Gd-DTPA injection]. A higher enhancement ratio suggests higher concentration of Gd-DTPA and higher permeability (disruption or immaturity) of the blood-CSF barrier. MRVision (MR Vision Co.) was used to display and perform measurements on all MR images.

RESULTS

BBB and Blood-CSF Barrier Assessment with T_1 WI and T_1 Mapping after Injection of Gd-DTPA

Typical T_1 WIs and quantitative T_1 maps for all groups are shown in Fig. 1. The brain size of the 1-week-old radiation-exposed rats (43.8 ± 2.6 mm²) was smaller than that of the 1-week-old normal rats (65.9 ± 2.3 mm²) ($P < 0.001$). Similarly, the brain size of the 2-week-old radiation-exposed rats (59.5 ± 4.3 mm²) was smaller than that of the 2-week-old normal rats (92.1 ± 4.2 mm²) ($P < 0.001$). There was also significant dilatation of the cerebral ventricles (Fig. 1-C1, 1-D1). Except in the ventricles, the CNS T_1 values of the 1-week-old rats were higher than those of the 2-week-old rats (compare Fig. 1-A3 to 1-B3 and 1-C3 to 1-D3). The T_1 values of the CNS decreased significantly after Gd-DTPA injection, especially for the 1-week-old groups (compare Fig. 1-A3 to 1-A4 and 1-C3 to 1-C4). For all groups, the signal from the scalp in the T_1 WIs was enhanced 42 min after Gd-DTPA administration (Fig. 1-A2, 1-B2, 1-C2, 1-D2).

Significant enhancement of the ventricles, indicating a leaky blood-CSF barrier, was observed in the normal (29 ± 4%, Fig. 1-A2) and radiation-exposed (30 ± 7%, Fig. 1-C2) 1-week-old rats compared to both 2-week-old groups ($P < 0.001$). No enhancement of the ventricles was observed in the normal (6 ± 3%, Fig. 1-B2) and radiation-exposed (5 ± 2%, Fig. 1-D2) 2-week-old rats.

Figure 2 presents a longitudinal observation of the normalized T_1 ratio in the cortex after injection of Gd-DTPA. In the normal animals, the normalized T_1 ratio of the 1-week-old rats was significantly lower than that of the 2-week-old rats from 27 min until 37 min after the injection ($P < 0.001$) (Fig. 2A). The normalized T_1 ratios decreased rapidly 5 min after Gd-DTPA administration in both the 1- and 2-week-old normal rats. Thereafter, the normalized T_1 ratio of the 2-week-old rats slowly recovered, whereas that of the 1-week-old rats continued to decrease (Fig. 2A).

For the radiation-exposed animals, the normalized T_1 ratio of the 1-week-old rats was lower than that of the 2-week-old rats from 5 min after the Gd-DTPA injection until 37 min ($P < 0.001$) (Fig. 2B). Comparison of the

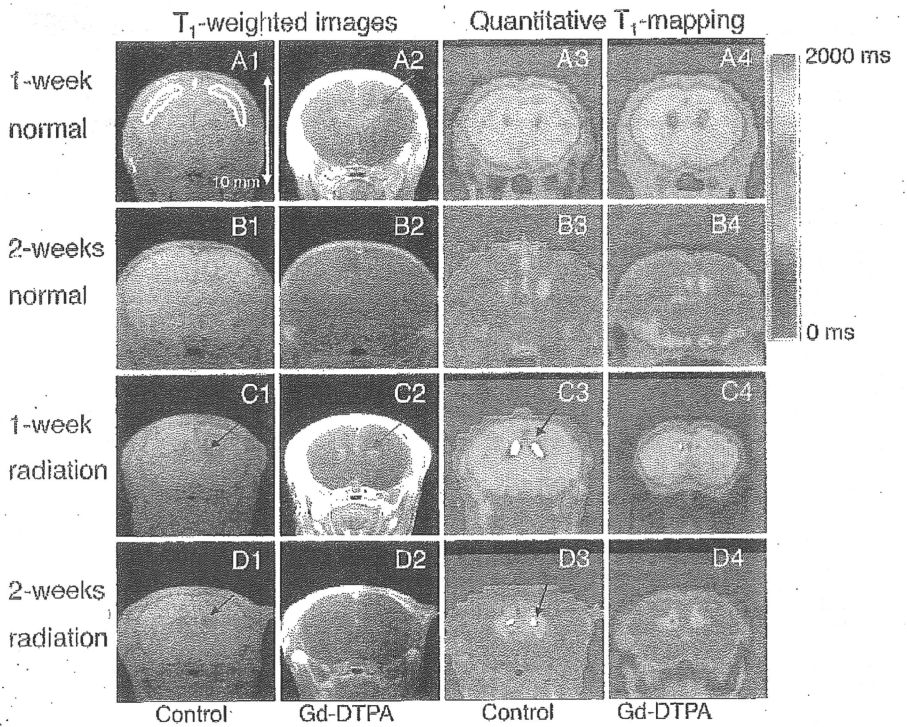

FIG. 1. Typical T_1-weighted MRI and T_1 maps. The grayscale images show typical coronal T_1-weighted images (TR/TE = 400 ms /9.57 ms, white arrows = 10 mm) and the color images show typical coronal quantitative T_1 maps (TR/TE = 10,000 ms/10 ms) for the same slice. The first and third columns are control images before Gd-DTPA administration, while the second and fourth columns are images after Gd-DTPA administration. The white lines in panel A1 delineate the chosen ROI. The black arrows (panels C1, C3, D1, D3) point to ventricle dilatation in the radiation-exposed groups. The red arrows in panels A2 and C2 indicate Gd-DTPA signal enhancement in the T_1-weighted images. The brain size of the radiation-exposed groups is clearly smaller than that of the normal animals.

normalized T_1 ratio of the 1-week-old normal and radiation-exposed rats found that the ratio of the normal group was significantly lower than that of the radiation-exposed group only at 37 min after Gd-DTPA injection ($P < 0.01$) (Fig. 2C). In the 2-week-old animals, the normalized T_1 ratio in the cortex of the normal rats was lower than that of the radiation-exposed rats from 11 min and up until 37 min after the Gd-DTPA injection ($P < 0.05$ at 16, 21, 27, 32 and 37 min, $P < 0.01$ at 11 min) (Fig. 2D).

BBB Assessment after Albumin Staining

Figure 3 shows a typical histology of the CNS after albumin staining. The density of albumin-positive cells was significantly higher in the cortex of the 1-week-old normal (Fig. 3A) and radiation-exposed rats (Fig. 3C) compared to the 2-week-old groups (Fig. 3B, D, E). Comparison of the fraction of albumin-positive stained cells for the 1-week-old normal and radiation-exposed rats showed that the density of positive cells in the radiation-exposed group was lower than in the normal rats ($P < 0.001$) (Fig. 3E).

Evaluation of Vessel Condition Using Perfusion Imaging and Immunohistochemical Staining

The cerebral vascular system of all rats was evaluated with MR angiography. In comparison to the normal rats (Fig. 4A–C), narrowing of the anterior cerebral artery

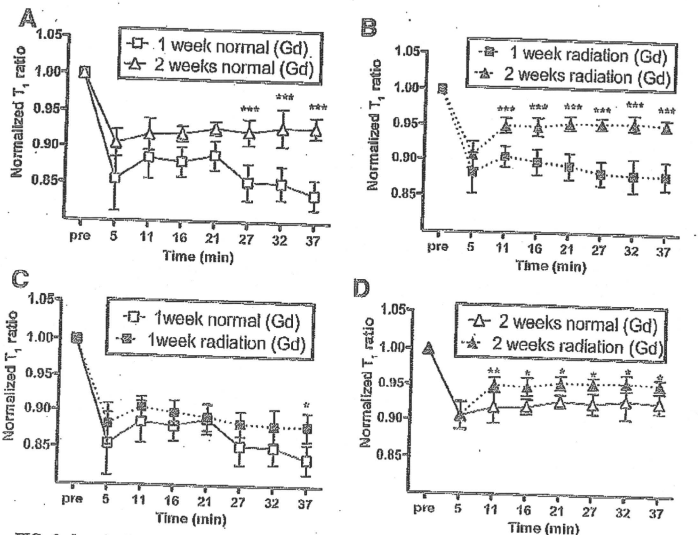

FIG. 2. Longitudinal observation of the normalized T_1 ratio in the cortex after Gd-DTPA injection. Data for (panel A) 1-week-old normal compared to 2-week-old normal, (panel B) 1-week-old radiation-exposed compared to 2-week-old radiation-exposed, (panel C) 1-week-old normal compared to 1-week-old radiation-exposed, and (panel D) 2-week-old normal compared to 2-week-old radiation-exposed are shown. The ROI was defined as the entire cortex (Fig. 1-A1). T_1 values were normalized using the first image of T_1 mapping before Gd-DTPA was introduced. Two-way ANOVA was used for statistical comparison ($^{*}P < 0.05$, $^{**}P < 0.01$, $^{***}P < 0.001$).

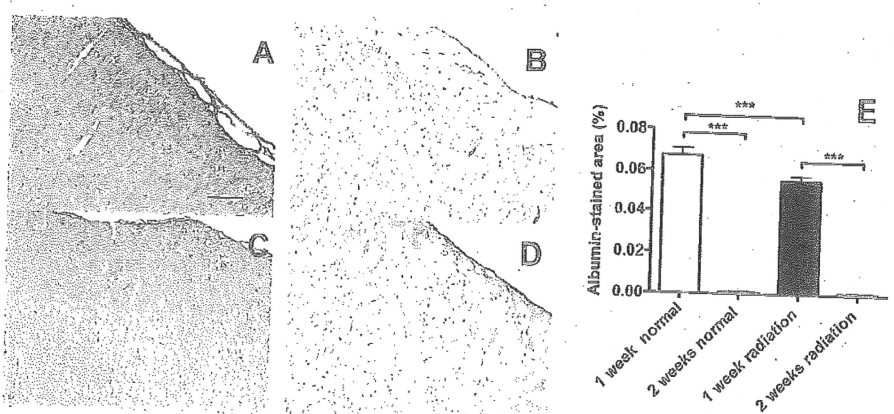

FIG. 3. Histology using albumin staining. Typical albumin-stained slices of the cortex (original magnification: 200×, black bar = 200 μm) are shown for 1-week-old normal (panel A), 2-week-old normal (panel B), 1-week-old radiation-exposed (panel C), and 2-week-old radiation-exposed (panel D) rats. The density of albumin-positive cells in the cortex is shown in panel E.

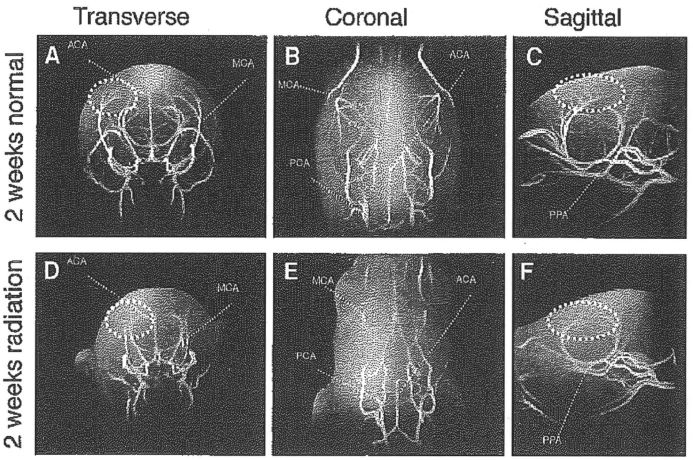

FIG. 4. Typical MR angiograph (TR/TE = 15 ms/2.4 ms, flip angle = 20°) is presented as a maximum-intensity projection. The cerebral arteries (ACA, MCA and PCA) of the radiation-exposed rat were clearly shorter than those of the normal rat. Also, the peripheral arteries were not clear in the radiation-exposed rat (dotted ellipse). ACA; anterior cerebral artery, PCA; posterior cerebral artery, MCA; middle cerebral artery, PPA; pterygo-palatine artery.

(ACA), posterior cerebral artery (PCA) and MCA were clearly observed for the radiation-exposed rats (Fig. 4D–F). The peripheral arteries were not clearly visible in the radiation-exposed rats. The diameter of the MCA at its origin was 0.24 ± 0.02 mm in the radiation-exposed rats and 0.38 ± 0.02 mm in the normal rats. The diameter of the MCA at its origin in the radiation-exposed rats was smaller than that in the normal rats ($P < 0.01$).

Figure 5 presents a typical quantitative perfusion map for the normal (Fig. 5-1A) and radiation-exposed (Fig. 5-1B) 2-week-old rats. Morphological dilatation of the ventricles was apparent in the perfusion images of radiation-exposed rats in areas corresponding to lowest CBF (Fig. 5-1B). CBF values for the 2-week-old normal and radiation-exposed rats were 206 ± 31 and 110 ± 15 ml/100 g/min, respectively. In the 2-week-old rats, the CBF of the radiation-exposed rats was significantly lower than that of the normal rats ($P < 0.01$) (Fig. 5C).

Laminin staining demonstrated the endothelial cell structure (Fig. 5D, E). In the 2-week-old rats, the density of laminin-positive cells in the radiation-exposed animals was significantly smaller than that in the normal animals (Fig. 5F) ($P < 0.05$). Similarly, in the 1-week-old rats, the density of laminin-positive cells of the radiation-exposed rats was significantly smaller than for the normal rats ($P < 0.001$) (Fig. 5F). A significant difference in the density of laminin-positive cells was also found between the two normal groups (49%: 1-week-old normal compared to 2-week-old normal, $P < 0.001$) and the two radiation-exposed groups (63%: 1-week-old radiation-exposed compared to 2-week-old radiation-exposed, $P < 0.001$), although these results can probably be attributed to developmental differences.

DISCUSSION

This study is the first to noninvasively evaluate CNS abnormalities in the rodent brain with MRI after prenatal X-ray exposure. We found that decreased CBF, indicating immature capillary development in the irradiated neonatal rats, can be identified using quantitative perfusion MRI. We observed angioarchitectonic abnormalities in the irradiated neonatal rats with MR angiography, and we were able to evaluate the development of the BBB and blood-CSF-barrier of 2-week-old irradiated rats noninvasively with Gd-enhanced MRI.

BBB and Blood CSF Evaluation in Neonatal Normal Rat.

The BBB has an important role as a "filter" that allows selective permeation of molecules to protect the CNS from toxic substances. The BBB of the neonatal rat brain is more permeable than that of adults (*14*), but it is completely formed at 2 or 3 weeks after birth (*20*). For these reasons we chose to compare the BBB of 1-week-

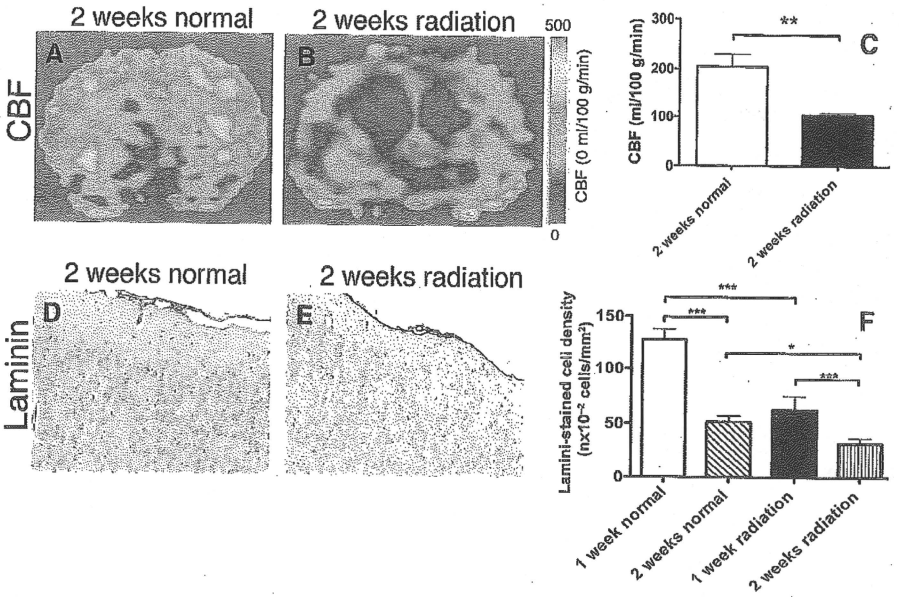

FIG. 5. Perfusion MRI experiments and laminin histology. Panels A and B: Typical quantitative perfusion maps (TR/TE = 18000 ms/26 ms) are shown for the 2-week-old normal (panel A) and 2-week-old radiation-exposed (panel B) groups without any contrast agent. Morphological ventricle dilatation was observed in the 2-week-old radiation-exposed animals (panel B). Panel C: CBFs for the 2-week-old normal and 2-week-old radiation-exposed groups. Panels D and E: Typical laminin-stained histological slices of the cortex for the 2-week-old normal (panel D) and 2-week-old radiation-exposed (panel E) groups (original magnification: 200×, black bar = 200 μm). Panel F: The density of laminin-positive cells for all groups.

old animals, when the development is incomplete, with the mature BBB of 2-week-old animals. When the BBB is immature, Gd-DTPA (*26, 27*) or albumin (*28*) can readily leak into the brain parenchyma so that Gd-DTPA MRI and albumin staining both reflect incomplete BBB development. Our Gd-DTPA study agreed well with the albumin staining (Fig. 3A, B), which agrees with the fact that the BBB in normal rats is formed primarily during the second week after birth (Fig. 2A) (*20*). Therefore, Gd-DTPA can be used to noninvasively determine whether the BBB development is normal in both irradiated and normal rats.

The epithelial cells in the choroid plexus and the arachnoid membrane in the ventricles form the blood-CSF barrier. Enhancement of the ventricles after Gd-DTPA administration indicates disruption or immaturity of the blood-CSF barrier. Enhancement of the ventricles in 1-week-old normal (Fig. 1-A2) and radiation-exposed (Fig. 1-C2) rats indicated immaturity of the blood-CSF barrier at this age. The unenhanced ventricles in the 2-week-old rats suggested that the blood-CSF barrier was well developed in both the normal (Fig. 1-B2) and radiation-exposed animals (Fig. 1-D2). Using destructive inspection, Sturrock found that the morphological development of the choroid plexus occurs between 11 and 14 days after birth (*29*). Our *in vivo* Gd-enhanced MRI results agreed with those results and suggest that radiation does not affect the development of the blood-CSF barrier. MRI with Gd-DTPA can be also used to noninvasively assess development of the blood-CSF barrier in normal and radiation-exposed rats during the second week after birth.

BBB Evaluation in Neonatally Irradiated Rats

Although some authors found that BBB permeability in adult rats was altered after radiation exposure (*10, 11*), there are no previous reports evaluating the BBB permeability of rats prenatally exposed to radiation. In our prenatally irradiated rats, the normalized T_1 ratio of the 1-week-old rats was smaller than that of the 2-week-

old rats (Fig. 2B). In addition, the normalized T_1 ratio of the 2-week-old normal rats was smaller than that of the 2-week-old radiation-exposed rats (Fig. 2D). These results suggest that the BBB permeability of the radiation-exposed 2-week-old rats was much smaller than that of the 1-week-old radiation-exposed rats. Moreover, albumin staining showed that BBB permeability decreased significantly in the 2-week-old radiation-exposed rats compared with the 1-week-old rats (Fig. 3C, D), suggesting that the BBB can form even after prenatal radiation exposure.

Assessment of Vasculature and Microcirculation

Arterial vasculature and blood microcirculation after prenatal radiation exposure were evaluated by quantitative perfusion MRI and MR angiography (*30*). Angiography of the irradiated rats demonstrated that branching arteries from the ACA, MCA and PCA were clearly malformed (Fig. 4). X irradiation (2.5 Gy) of the CNS may lead to malformation of the vascular endothelium in the adult rat (*9*). A recent *in vitro* study found that radiation (over 50 Gy) applied to brain slices induced acute-phase apoptosis of endothelial cells 24 h after irradiation, and microvessel injury was also detected in the CNS of 16-week-old mice (*8*). Similar to these *in vitro* reports (*5*), our results suggest that disturbance of vascular development was triggered by prenatal X-ray exposure, and this may be linked to whole-brain atrophy. However, because a fetus is more sensitive to radiation than an adult (*13*), we used a single 1.5-Gy dose of radiation, which is quite low compared to previous studies (*8, 9*).

Lo *et al.* examined the chronic effects of a single high dose (60 Gy) of X rays and found significant reductions in regional CBF ratios in the cortex of irradiated adult rabbits (*31*). Yoshii also reported that chronic damage [such as necrosis (encephalomalacia), atrophy, cell infiltration and telangiectatic vascular change] to the arterial system was observed in serial brain sections after whole-brain X irradiation (13–60 Gy) in adult mice (*32*). We evaluated the cortical CBF using quantitative perfusion MRI (*23, 33, 34*). The CBF of the radiation-exposed rats was significantly smaller than that of the normal rats (Fig. 5A, B). In our histological experiments, laminin staining highlighted the regions where the volume of vascular endothelial cells decreased after prenatal X irradiation (Fig. 5D–F). Even though the dose (1.5 Gy) was quite low compared to those used in previous experiments on adult rats (13–60 Gy), our results indicate that X radiation causes a developmental disorder in the vasculature of the neonatal rat brain.

In conclusion, we noninvasively and quantitatively evaluated prenatal X-ray-induced CNS abnormalities. Decreased CBF and angioarchitectonic abnormalities were the main alterations observed. The BBB and blood-CSF barrier were normally formed by 2 weeks after birth in both the radiation-exposed and normal rats. Because the techniques we used are also available for clinical MRI scanners, the same noninvasive and quantitative imaging methodology can be applied directly to humans. In addition, the angioarchitectonic abnormalities revealed by our imaging technology provides important diagnostic information to assess the condition of patients during the early stages of life after prenatal exposure due to a radiation accident or radiation therapy received during pregnancy.

ACKNOWLEDGMENTS

The authors would like to thank Ms. Sayaka Shibata and Mr. Takeo Shimomura (National Institute of Radiological Sciences, Japan) for technical assistance. This work was partly supported by Grants-in-Aid for Scientific Research (Kakenhi) of the Japan Society for the Promotion of Science (JSPS).

Received: January 8, 2010; accepted: September 7, 2010; published online: November 10, 2010

REFERENCES

1. W. J. Blot, Growth and development following prenatal and childhood exposure to atomic radiation. *J. Radiat. Res. (Tokyo)* **16** (Suppl.), 82–88 (1975).
2. M. Otake, W. J. Schull and H. Yoshimaru, A review of forty-five years study of Hiroshima and Nagasaki atomic bomb survivors. Brain damage among the prenatally exposed. *J. Radiat. Res. (Tokyo)* **32** (Suppl.), 249–264 (1991).
3. M. Otake and W. J. Schull, Radiation-related brain damage and growth retardation among the prenatally exposed atomic bomb survivors. *Int. J. Radiat. Biol.* **74**, 159–171 (1998).
4. K. Hoshino and Y. Kamcyama, Developmental-stage-dependent radiosensitivity of neural cells in the ventricular zone of telencephalon in mouse and rat fetuses. *Teratology* **37**, 257–262 (1988).
5. N. Takai, X. Z. Sun, K. Ando, K. Mishima and S. Takahashi, Ectopic neurons in the hippocampus may be a cause of learning disability after prenatal exposure to X-rays in rats. *J. Radiat. Res. (Tokyo)* **45**, 563–569 (2004).
6. X. Z. Sun, S. Takahashi, Y. Kubota, H. Sato, C. Cui, Y. Fukui and M. Inouye, Types and three-dimensional distribution of neuronal ectopias in the brain of mice prenatally subjected to X-irradiation. *J. Radiat. Res. (Tokyo)* **43**, 89–98 (2002).
7. D. G. Baker and R. J. Krochak, The response of the microvascular system to radiation: a review. *Cancer Invest.* **7**, 287–294 (1989).
8. L. A. Pena, Z. Fuks and R. N. Kolesnick, Radiation-induced apoptosis of endothelial cells in the murine central nervous system: protection by fibroblast growth factor and sphingomyelinase deficiency. *Cancer Res.* **60**, 321–327 (2000).
9. N. V. Ljubimova, M. K. Levitman, E. D. Plotnikova and L. Eidus, Endothelial cell population dynamics in rat brain after local irradiation. *Br. J. Radiol.* **64**, 934–940 (1991).
10. T. Siegal and M. R. Pfeffer, Radiation-induced changes in the profile of spinal cord serotonin, prostaglandin synthesis, and vascular permeability. *Int. J. Radiat. Oncol. Biol. Phys.* **31**, 57–64 (1995).
11. P. Rubin, D. M. Gash, J. T. Hansen, D. F. Nelson and J. P. Williams, Disruption of the blood-brain barrier as the primary effect of CNS irradiation. *Radiother. Oncol.* **31**, 51–60 (1994).

12. H. Yuan, M. W. Gaber, K. Boyd, C. M. Wilson, M. F. Kiani and T. E. Merchant, Effects of fractionated radiation on the brain vasculature in a murine model: blood-brain barrier permeability, astrocyte proliferation, and ultrastructural changes. *Int. J. Radiat. Oncol. Biol. Phys.* 66, 860–866 (2006).

13. B. F. Kimler, Prenatal irradiation: a major concern for the developing brain. *Int. J. Radiat. Biol.* 73, 423–434 (1998).

14. D. W. Caley and D. S. Maxwell, Development of the blood vessels and extracellular spaces during postnatal maturation of rat cerebral cortex. *J. Comp. Neurol.* 138, 31–47 (1970).

15. M. E. Philippens, G. Gambarota, A. J. van der Kogel and A. Heerschap, Radiation effects in the rat spinal cord: evaluation with apparent diffusion coefficient versus T2 at serial MR imaging. *Radiology* 250, 387–397 (2009).

16. Y. L. Chan, D. K. Yeung, S. F. Leung and P. N. Chan, Diffusion-weighted magnetic resonance imaging in radiation-induced cerebral necrosis. Apparent diffusion coefficient in lesion components. *J. Comput. Assist. Tomogr.* 27, 674–680 (2003).

17. M. W. Munter, C. P. Karger, W. Reith, H. M. Schneider, P. Peschke and J. Debus, Delayed vascular injury after single high-dose irradiation in the rat brain: histologic immunohistochemical, and angiographic studies. *Radiology* 212, 475–482 (1999).

18. Y. L. Chan, D. K. Yeung, S. F. Leung, S. F. Lee and A. S. Ching, Dynamic susceptibility contrast-enhanced perfusion MR imaging in late radiation-induced injury of the brain. *Acta Neurochir. Suppl.* 95, 173–175 (2005).

19. K. H. Chuang and A. Koretsky, Improved neuronal tract tracing using manganese enhanced magnetic resonance imaging with fast T(1) mapping. *Magn. Reson. Med.* 55, 604–611 (2006).

20. A. M. Butt, H. C. Jones and N. J. Abbott, Electrical resistance across the blood-brain barrier in anaesthetized rats: a developmental study. *J. Physiol.* 429, 47–62 (1990).

21. T. Hayashi, Y. Kusunoki, M. Hakoda, Y. Morishita, Y. Kubo, M. Maki, F. Kasagi, K. Kodama, D. G. Macphee and S. Kyoizumi, Radiation dose-dependent increases in inflammatory response markers in A-bomb survivors. *Int. J. Radiat. Biol.* 79, 129–136 (2003).

22. G. Paxinos and C. Watson, *The Rat Brain in Stereotaxic Coordinates*. Academic Press, San Diego, 1998.

23. S. G. Kim, Quantification of relative cerebral blood flow change by flow-sensitive alternating inversion recovery (FAIR) technique: application to functional mapping. *Magn. Reson. Med.* 34, 293–301 (1995).

24. T. Nitta, M. Hata, S. Gotoh, Y. Seo, H. Sasaki, N. Hashimoto, M. Furuse and S. Tsukita, Size-selective loosening of the blood-brain barrier in claudin-5-deficient mice. *J. Cell Biol.* 161, 653–660 (2003).

25. Y. Q. Li, P. Chen, A. Haimovitz-Friedman, R. M. Reilly and C. S. Wong, Endothelial apoptosis initiates acute blood-brain barrier disruption after ionizing radiation. *Cancer Res.* 63, 5950–5956 (2003).

26. V. M. Runge, J. A. Clanton, A. C. Price, C. J. Wehr, W. A. Herzer, C. L. Partain and A. E. James, Jr., The use of Gd DTPA as a perfusion agent and marker of blood-brain barrier disruption. *Magn. Reson. Imaging* 3, 43–55 (1985).

27. H. B. Larsson and P. S. Tofts, Measurement of blood-brain barrier permeability using dynamic Gd-DTPA scanning—a comparison of methods. *Magn. Reson. Med.* 24, 174–176 (1992).

28. A. W. Vorbrodt and D. H. Dobrogowska, Immunocytochemical evaluation of blood-brain barrier to endogenous albumin in adult, newborn and aged mice. *Fol. Histochem. Cytobiol.* 32, 63–70 (1994).

29. R. R. Sturrock, A morphological study of the development of the mouse choroid plexus. *J. Anat.* 129, 777–793 (1979).

30. T. Reese, D. Bochelen, A. Sauter, N. Beckmann and M. Rudin, Magnetic resonance angiography of the rat cerebrovascular system without the use of contrast agents. *NMR Biomed.* 12, 189–196 (1999).

31. E. H. Lo, K. A. Frankel, G. K. Steinberg, R. L. DeLaPaz and J. I. Fabrikant, High-dose single-fraction brain irradiation: MRI, cerebral blood flow, electrophysiological, and histological studies. *Int. J. Radiat. Oncol. Biol. Phys.* 22, 47–55 (1992).

32. Y. Yoshii and T. L. Phillips, Late vascular effects of whole brain X-irradiation in the mouse. *Acta Neurochir. (Wien)* 64, 87–102 (1982).

33. J. A. Detre, W. Zhang, D. A. Roberts, A. C. Silva, D. S. Williams, D. J. Grandis, A. P. Koretsky and J. S. Leigh, Tissue specific perfusion imaging using arterial spin labeling. *NMR Biomed.* 7, 75–82 (1994).

34. H. S. Kim, S. Y. Kim and J. M. Kim, Underestimation of cerebral perfusion on flow-sensitive alternating inversion recovery image: semiquantitative evaluation with time-to-peak values. *AJNR Am. J. Neuroradiol.* 28, 2008–2013 (2007).